Revisiting the Role of the Streaming Instability for the Cosmic-Ray Spectrum in the GeV-to-TeV Range

The Astrophysical Journal, 1001:7 (12pp), 2026 April 10 https://doi.org/10.3847/1538-4357/ae4ec4

Revisiting the Role of the Streaming Instability for the Cosmic-Ray Spectrum in the GeV-to-TeV Range

Linh Han Thanh[1,2], Julien Dörner[1,2], Julia Becker Tjus[1,2,3], Horst Fichtner[1,2], and Elena Amato[4]
[1] Ruhr University Bochum, Faculty for Physics & Astronomy, Theoretical Physics IV, Plasma-Astroparticle Physics, Bochum, Germany
[2] Ruhr Astroparticle and Plasma Physics Center (RAPP Center), Ruhr University Bochum, Germany
[3] Department of Space, Earth and Environment, Chalmers University of Technology, SE-412 96 Gothenburg, Sweden
[4] NAF-Osservatorio Astrofisico di Arcetri, Universita degli Studi di Firenze, Italy
Received 2025 December 15; revised 2026 March 5; accepted 2026 March 5; published 2026 April 1

Abstract

A complete understanding of the cosmic-ray energy spectrum remains a challenge to theory that must be met by comprehensive modeling efforts. One of these is the subject of the present study, namely, an explanation of the recently discovered spectral hardening at ∼300 GeV with self-consistently treated cosmic-ray diffusion, where self-generated waves resulting from the streaming instability impact the diffusion of high-energy particles. We revisit the corresponding model by P. Blasi et al., perform an extensive parameter study, and determine an optimal range of parameters that best fit the cosmic-ray data. We conclude that self-consistently treated cosmic-ray transport remains a competitive alternative to explain the spectral hardening of the cosmic-ray energy spectrum at a few hundred GeV.

Unified Astronomy Thesaurus concepts: Galactic cosmic rays (567); Interstellar magnetic fields (845); Interstellar medium (847); Plasma astrophysics (1261)

1. Introduction

Understanding the energy spectrum of cosmic rays in all its complexity remains an important task of contemporary astrophysics, because it contains information about the acceleration as well as propagation of cosmic rays within the Galaxy and beyond and about the physical properties of the media these high-energy particles traverse. For many years, the energy spectrum was considered to have a comparatively simple form mainly characterized by three different power laws (J. Becker Tjus & L. Merten 2020), namely, one in the range from ∼10 to ∼3×10^6 GeV as a result of (diffusive shock) acceleration at Galactic sources and subsequent propagation in the interstellar medium, a steeper one above the so-called knee up to the ankle at ∼4×10^9 GeV, and finally a third, again flatter one, beyond the ankle. While the origin of the range between the knee and the ankle is still under debate, the latter part of the spectrum is presumably comprised of extragalactic cosmic rays. These power-law sections of the spectrum are bordered at ultrahigh energies by the rather sharp "Greisen–Zatsepin–Kuzmin" cutoff (K. Greisen 1966; G. T. Zatsepin & V. A. Kuz'min 1966) and at the low-energy end, if observed at Earth, by a gradual flux decrease due to the so-called modulation caused by the heliosphere (M. S. Potgieter 1998).

Over the years, improved observations have revealed additional features in the cosmic-ray energy spectrum (see, e.g., S. Recchia & S. Gabici 2024). Above the "original" knee near 3×10^6 GeV, a "second knee" near 10^8 GeV has been identified (K.-H. Kampert 2013; P. Abreu et al. 2021) and is now considered as one of several element-specific knees (A. De Rújula 2019). Below the knee, measurements with the DAMPE satellite (Q. An et al. 2019) confirmed a spectral hardening at ∼300 GeV found before (by PAMELA, O. Adriani et al. 2011, as well as AMS-02, M. Aguilar et al. 2015) and led to the discovery of a softening at ∼13.6 TeV. These measurements were subsequently confirmed with CALET (O. Adriani et al. 2022).

The present study is devoted to the latter feature, i.e., the spectral hardening at ∼300 GeV that may be explained as an effect of cosmic-ray sources in the vicinity of the Sun (S. Bhadra et al. 2025; X.-L. Qian et al. 2025 and references therein), cosmic-ray transport in the interstellar medium (W. Liu et al. 2018; E. Silver & E. Orlando 2024 and references therein), deviations of the injection spectra of cosmic rays from a simple power law (see, e.g., P. L. Biermann et al. 2010; X. Pan & Q. Yuan 2023), or reacceleration of cosmic rays by weak shocks (S. Thoudam & J. R. Hörandel 2014). While the explanations by local sources and deviations in the source spectrum address the hardening and softening at the same time, self-consistent models of the cosmic-ray transport often address only the hardening. Out of these alternatives, we study the second by revisiting the idea that this spectral hardening is related to the streaming instability of cosmic rays, which was first studied in the context of spectral breaks in the cosmic-ray energy spectrum by P. Blasi et al. (2012). In contrast to test particle propagation models based on the assumption of a spatially dependent diffusion coefficient (W. Liu et al. 2018) with a possibly nonseparable energy dependence (N. Tomassetti 2012) or on the assumption of a spatially constant diffusion in combination with reacceleration and convection (E. Silver & E. Orlando 2024), P. Blasi et al. (2012) proposed a self-consistent approach taking into account the interaction of cosmic rays with self-generated turbulence.

The paper is organized as follows. After we describe and justify the model equations in Section 2, we present a comprehensive parameter study in Section 3. This is followed in Section 4 by a determination of a parameter combination

best-fitting the cosmic-ray data. In Section 5, all findings are critically discussed, and corresponding conclusions are drawn.

2. Model Equations

Following the work of P. Blasi et al. (2012) and R. Aloisio & P. Blasi (2013), we consider cosmic-ray particles, accelerated by supernova (SN) remnants and traveling along the field lines of a large-scale magnetic field $\boldsymbol{B_0} = B_0\hat{z}$. Alongside the regular field, the surrounding plasma exhibits a weakly turbulent component, δB, in the form of Alfvén waves. Via electromagnetic interaction, these waves can serve as scattering centers for the cosmic-ray particles and can be enhanced by the particles in this process. As the wave enhancement depends on the particle distribution, which itself is affected by the Alfvén waves, this so-called streaming instability can be treated with a coupled system of differential equations, which we introduce in the following.

As a first step, we adapt a one-dimensional flux-tube approximation, where purely parallel diffusion is considered under the assumption that processes influencing the perpendicular direction leave the parallel part unaffected. The steady-state transport equation describing the cosmic-ray particles then reads

$$-\frac{\partial}{\partial z}\left[D\frac{\partial f}{\partial z}\right] + v_{\rm A}\frac{\partial f}{\partial z} - \frac{dv_{\rm A}}{dz}\frac{p}{3}\frac{\partial f}{\partial p} = q_{\rm CR}(p, z) = q_0(p)\delta(z), \quad (1)$$

where the terms denote spatial diffusion with a momentum-dependent diffusion coefficient $D = D(p)$, advection with the Alfvén speed $v_{\rm A} = B_0/\sqrt{4\pi n_i m_i}$, adiabatic expansion/compression, and a source, respectively. The isotropic phase-space distribution function $f(p, z)$ is normalized to the total number of particles in the process, $N = \int dp\, dV\, 4\pi p^2 f(p, z)$, where dV denotes a volume element.

Second, the shock-accelerated particles are assumed to be injected with a power-law spectrum, homogeneously distributed over the Galactic disk, i.e., at $z = 0$ for the disk structure oriented in (x, y),

$$q_0(p) = A\left(\frac{p}{mc}\right)^{-\alpha}.$$

The normalization constant A is determined by the part of the energy of the SN explosion that is transferred to the cosmic rays. A fraction $\xi_{\rm CR}$ of the total kinetic energy released by the SN, $E_{\rm SN}$, bears upon the acceleration of particles, multiplication with the SN occurrence rate $\mathcal{R}_{\rm SN}$ yields the temporally averaged abundance, and division by the area of the Galactic disk, $\pi R_{\rm d}^2$, accounts for a spatial average. We note that $R_{\rm d}$ refers to the region of cosmic-ray sources, which differs from the actual extent of the Milky Way (see, e.g., P. Blasi & E. Amato 2012). Let

$$\epsilon(p) = (\sqrt{(p/(mc))^2 + 1} - 1)mc^2 \quad (2)$$

denote the momentum dependence of the cosmic-ray kinetic energy. Here, we will only consider protons, as the cosmic-ray spectrum in the considered energy range from GeV to TeV is dominated by protons, and a comparison of the modeled to the directly measured proton flux is possible. We leave it to future work to add heavier elements, as other effects, like a different injecting population, need to be considered; see, e.g., P. L. Biermann et al. (2010). Then, the normalization reads

$$\int q_0(p)\,\epsilon(p)\,d^3p = A\int_0^\infty \left(\frac{p}{mc}\right)^{-\alpha}\epsilon(p)4\pi p^2\,dp = \frac{\xi_{\rm CR}E_{\rm SN}\mathcal{R}_{\rm SN}}{\pi R_{\rm d}^2}. \quad (3)$$

After identifying

$$\mathcal{I}(\alpha) = \int_0^\infty \left(\frac{p}{mc}\right)^{-\alpha} 4\pi p^2\left[\sqrt{\left(\frac{p}{mc}\right)^2 + 1} - 1\right]mc^2\,dp = 4\pi\int_0^\infty x^{2-\alpha}(\sqrt{x^2+1} - 1)\,dx, \quad (4)$$

where in the last step we substituted $x = p/(mc)$, one finds for the normalization constant

$$A = \frac{\xi_{\rm CR}E_{\rm SN}\mathcal{R}_{\rm SN}}{\pi R_{\rm d}^2\mathcal{I}(\alpha)c(mc)^4} = 4\times 10^{36}\,{\rm cm^{-5}\,g^{-3}\,s^2}\left(\frac{\xi_{\rm CR}}{0.1}\right)\left(\frac{E_{\rm SN}}{10^{51}\,{\rm erg}}\right) \times \left(\frac{\mathcal{R}_{\rm SN}}{(30\,{\rm yr})^{-1}}\right)\left(\frac{R_{\rm d}}{10\,{\rm kpc}}\right)^{-2}\left(\frac{\mathcal{I}(\alpha)}{\mathcal{I}(4.3)}\right)^{-1}. \quad (5)$$

Note that the integral in $\mathcal{I}(\alpha)$ diverges for $\alpha \leqslant 4$.

Analogously to the original reference, we further assume that the spatial diffusion coefficient $D(p)$ as well as the Alfvén wave speed $v_{\rm A}$ are independent of the z-coordinate and only demand that the Alfvén waves propagate away from the disk at $z = 0$ both below and above, which corresponds to $dv_{\rm A}/dz = 2v_{\rm A}\delta(z)$.

The diffusion coefficient is determined by the magnetic field perturbations δB propagating as transversal Alfvén waves, which can resonantly interact with cosmic-ray particles. Any particle that by coincidence traverses a distance of an Alfvén wavelength during one gyration experiences a constant Lorentz force directed parallel to the $\boldsymbol{B}_0$ field and, as a consequence, is scattered. The resonance condition, therefore, is $k = 1/r_{\rm L} = qB_0/(pc)$, where k denotes the wavenumber, $r_{\rm L}$ is the Larmor radius of a particle, and q is its charge (this is a common simplification that we discuss in the Appendix). Third, assuming the turbulence level to be low, $\delta B \ll B_0$, the parallel diffusion coefficient can be written as

$$D(p) = \frac{1}{3}r_{\rm L}(p)v(p)\frac{1}{kW(k)}, \quad (6)$$

with the Bohm diffusion coefficient $D_{\rm B} = r_{\rm L}v/3$ as the limit of most efficient scattering (A. Shalchi 2009). The spectral power $W(k)$ is normalized by the turbulence level η such that

$$\int_{k_0}^\infty dk\; W(k) = \eta = \frac{\delta B^2}{B_0^2}. \quad (7)$$

Not only do the waves have an effect on the cosmic rays, and vice versa, but, likewise, wave–wave interactions can occur, not connected to cosmic rays. As two countermoving fluctuations encounter each other, they will tend to break up into smaller "eddies" due to nonlinear couplings. C. E. Leith (1967) and Y. Zhou & W. H. Matthaeus (1990) suggest that the net effect of all these interactions can be considered to be a local energy transfer in k-space. We therefore describe as a fourth step the evolution of the wave spectrum via a diffusion

ansatz,

$$-\frac{\partial}{\partial k}\left[D_{kk}\frac{\partial W}{\partial k}\right]-\Gamma_{\rm CR}W=q_W(k), \tag{8}$$

where we take into account—from left to right—diffusion of the spectral energy density, wave growth, and an injecting source. The wave diffusion coefficient is determined by $D_{kk}=k^2/\tau_s$, where the spectral energy transfer time is related to the triple correlation time τ_3 and the nonlinear or eddy turnover time $\tau_{\rm nl}$ through $\tau_3\tau_s=c_{\rm K}^{-1}\tau_{\rm nl}^2$. We refer to the constant $c_{\rm K}$ as the Kolmogorov constant.

Like J. A. Miller & D. A. Roberts (1995), we consider here the Kolmogorov and Kraichnan phenomenology. In the former case, the triple correlation time τ_3 is assumed to be of the order of the eddy turnover time, $\tau_{3,\rm Kolm}=\tau_{\rm nl}=\lambda/\delta v$, whereas Kraichnan allows for the magnetic field to take part, yielding $\tau_{3,\rm Kraich}=\lambda/v_{\rm A}$. Taking into account that the velocity fluctuations relate to the Alfvén speed, as do the magnetic field fluctuations to the average magnetic field, $\delta v^2/v_{\rm A}^2=\delta B^2/B_0^2$, and that $\lambda\approx 1/k$, we can, analogously to R. Aloisio & P. Blasi (2013), write

$$D_{kk}=c_{\rm K}v_{\rm A}k^{\alpha_1}W(k)^{\alpha_2}, \tag{9}$$

with $(\alpha_1,\ \alpha_2)=(7/2,\ 1/2)$ in the case of Kolmogorov phenomenology and (4, 1) for Kraichnan. The first term in Equation (8) consequently describes wave cascading.

Wave growth, in our model, occurs due to the above-mentioned streaming instability, as particles resonantly interact with and get scattered by Alfvén waves. For example, R. Kulsrud & W. P. Pearce (1969) state that the interaction is, on a larger scale, associated with a momentum transfer. Given an isotropic distribution, the effect of momentum loss and gain by the particles would balance. However, in the presence of a gradient, the streaming instability can occur, leading to wave growth. The associated growth rate for our purpose can be obtained by pitch-angle averaging the expression given by J. Skilling (1971),

$$\Gamma_{\rm CR}(k)=\frac{16\pi^2}{3}\frac{v_A}{kW(k)B_0^2}\left[p^4v(p)\frac{\partial f}{\partial z}\right]_{p=qB_0/kc}, \tag{10}$$

where $v(p)$ is the speed of a particle with momentum p and $\partial f/\partial z$ is the gradient in z-direction. The source term of Equation (8) in our setup is considered to be $q_W(k)\propto\eta\delta(k-k_0)$, injecting turbulence only on an outer scale k_0^{-1}. Without wave growth, i.e., by disregarding the term $\Gamma_{\rm CR}W$, this ansatz leads to a power-law-shaped wave spectrum $W=W_0(k/k_0)^{-s}$, with $s=(\alpha_1-1)/(\alpha_2+1)$.

The system of Equations (1) and (8) is nonlinear for the diffusion coefficient in the particles' transport equation being dependent on the wave spectrum through Equation (6) and the wave spectrum in turn being determined by the particle distribution function through the wave growth (Equation (10)). Owing to the simplifying assumptions, we can find an analytical solution to the particles' transport equation. Imposing the boundary conditions $f(z=\pm H)=0$, where H denotes the Galactic height, it reads

$$f(z,p)=f_0(p)\frac{1-e^{-\zeta(1-|z|/H)}}{1-e^{-\zeta}},\quad \zeta(p)\equiv\frac{v_{\rm A}H}{D(p)}. \tag{11}$$

The momentum-dependent part $f_0(p)$ can be found by integrating Equation (1) in the range $z=(0^-{-}0^+)$,

$$-2D(p)\left[\frac{\partial f}{\partial z}\right]_{z=0^+}-\frac{2}{3}v_{\rm A}p\frac{df_0}{dp}=q_0(p), \tag{12}$$

from which, in turn, an implicit solution can be derived as

$$f_0(p)=\frac{3}{2v_{\rm A}}\int_p^\infty\frac{dp''\,q_0(p'')}{p''}\times\exp\left[\int_p^{p''}\frac{3\,dp'}{p'(1-\exp[\zeta(p)])}\right]. \tag{13}$$

For this, we used that

$$\left[\frac{\partial f}{\partial z}\right]_{z=0^+}=\frac{v_{\rm A}f_0(p)}{D(p)}\frac{1}{1-\exp[\zeta(p)]}, \tag{14}$$

obtained by spatially differentiating Equation (11) and, with this derivative inserted, integrating Equation (12).

Likewise, an implicit solution to the wave Equation (8) can be found after integrating twice,

$$W(k)=\left[\left(-\frac{1+\alpha_2}{c_{\rm K}v_{\rm A}}\int_k^\infty\frac{dk'}{k'^{\alpha_1}}\int_{k_0}^{k'}dk''\,\Gamma_{\rm CR}(k'')W(k'')\right)+(c_3k^{1-\alpha_1})\right]^{\frac{1}{1+\alpha_2}}. \tag{15}$$

The integration constant c_3 here is determined by the requirement that in the absence of resonating cosmic-ray particles, the expected spectra, namely, Kolmogorov- or Kraichnan-like, are found. Then, we find $c_3=W_0^{1+\alpha_2}k_0^{\alpha_1-1}$ with $W_0=(s-1)\,k_0^{-1}\eta$ and the index $s=(\alpha_1-1)/(\alpha_2+1)$.

We solve the coupled differential Equations (1) and (8) by numerically integrating the implicit solutions (Equations (13) and (15)) with a trapezoidal method. In concrete terms, we divide each integral into 2×10^6 narrow intervals. Each of the inner integrals are solved with the SciPy (P. Virtanen et al. 2020) built-in `cumulative trapezoid` method, whereas the outer integrals are solved with the SciPy `trapezoid` methods for momentum p and wavenumber k in the ranges $[10^{-2},\ 10^7]$ GeV c^{-1} and $[k_0,\ 10^{-10}]$ cm^{-1}, respectively. In order to minimize the runtime, the implicit solutions are evaluated at 300 points, which we note is less than the number of integrands, and interpolated in between. As starting conditions, we take the distribution function to be $f_{i=0}(p)=q_0(p)H/(2D(p))$ and assume a wave spectrum according to $W_{i=0}=W_0(k/k_0)^{-s}$. The integrations are repeated in such a way that f_i is calculated according to Equation (13) with $D(p)$ taken from the previous iteration, $f_i(D_{i-1})$. Hereafter, W_i is computed as in Equation (15), where $\partial f/\partial z$ is derived via Equation (14) with $f(p)$ taken from the same iteration, $W_i(f_i)$. This iterative procedure is repeated until convergence is reached, which for our purposes is given when the maximal relative deviation of two consecutive iterations, $\|f_i/f_{i-1}\|_{\rm max}$ and $\|W_i/W_{i-1}\|_{\rm max}$, amounts to less than 0.5%.

3. Quantitative Parameter Study

Having introduced the model, there are different dependencies that are useful to investigate prior to performing a systematic Markov Chain Monte Carlo (MCMC) fit. We fix the values for

the Galactic height H and the turbulence injection scale k_0^{-1} to typical values of $H = 4$ kpc and $k_0^{-1} = 50$ pc. The remaining parameters are the large-scale magnetic field strength B_0; its turbulence level η; the Alfvén speed v_A; the cosmic-ray injection slope α; the factor A, which itself is composed of multiple quantities; and the Kolmogorov constant c_K.

In order to roughly estimate the expected position of the spectral break caused by the streaming instability, we use the fact that the wave growth rate Γ_{CR}, given by Equation (10), needs to prevail over the counteracting wave cascading with $\Gamma_D \approx D_{kk}/k^2$. Approximating $\partial f/\partial z \approx -f_0/H$ with the distribution function chosen to be the solution to the diffusion-dominated transport equation at $z = 0$, $f_0 = q_0 H/(2D)$, and where the diffusion coefficient according to Equation (6) is determined by the external wave spectrum $W = (s-1)k_0^{s-1}\eta k^{-s}$, the momentum at which a transition from wave cascading to growth occurs can be calculated as

$$p_{\rm break} = \left\{ \frac{8\pi^2}{B_0^2 c_K} k_0^{\alpha_2(1-s)} [\eta(s-1)]^{-\alpha_2} \times A(mc)^{\alpha} \left(\frac{qB_0}{c}\right)^{3-\alpha_1+s\alpha_2} \right\}^{\frac{1}{\alpha+s\alpha 2-\alpha_1-1}}. \quad (16)$$

We display the different dependencies of the break energies on various parameters in Figure 1. In almost all cases, the break energies are higher with the Kraichnan-like cascade. An increase of the injection factor A leads to increasing break energies. The opposite is true for the remaining parameters. The visible changes of slope are due to the transition from the relativistic to the nonrelativistic regime.

In the following, we perform a quantitative parameter study to obtain a first idea of the various parameters' influences on the particle distribution function and the wave spectrum. The default parameter set is chosen such that the models resemble observational cosmic-ray data (Figure 2). From there, we successively vary one parameter at a time. Figures 3 and 4 show the results for a Kolmogorov and a Kraichnan phenomenology, respectively. Figure 3 shows the behavior of the cosmic-ray energy spectrum (left) and magnetic wave spectrum (right) at the variation of the different parameters. The estimated break energy is indicated in Figures 3 and 4 by vertical lines. The following trends are the same for Figure 4.

1. *Normalization of the cosmic-ray injection spectrum A.* Given the wide range of the normalization constant A, we see that apart from shifting the particle spectrum by a constant factor of $10^{0.5}$—since the absolute number of particles in the system is being changed—the energy range in which streaming instability occurs is also shifted. With increasing values of A, the energies at which wave growth becomes the predominant effect also increase. This is visible both in the spectral break of the particle distribution and even more clearly in the wave spectrum.
2. *Variation of* α. The variation of the spectral index α mainly affects the steepness of the particle distribution function, while all functions almost meet in one point at about $mc(\alpha_i/\alpha_j)^{1/(\alpha_j-\alpha_i)} \approx 0.26$ GeV, taking the highest index, α_j, and lowest, α_i, under consideration in the advection-dominated solution. A lower value of α corresponds to a flatter distribution f (and thus dN/dE) and more particles that are available to resonantly interact with the abundant magnetic field perturbations. With decreasing spectral index, growth sets in at higher energies. In addition, the level of wave power at the high-energy end of the streaming instability regime remains higher. For the two lowest values of α, an even

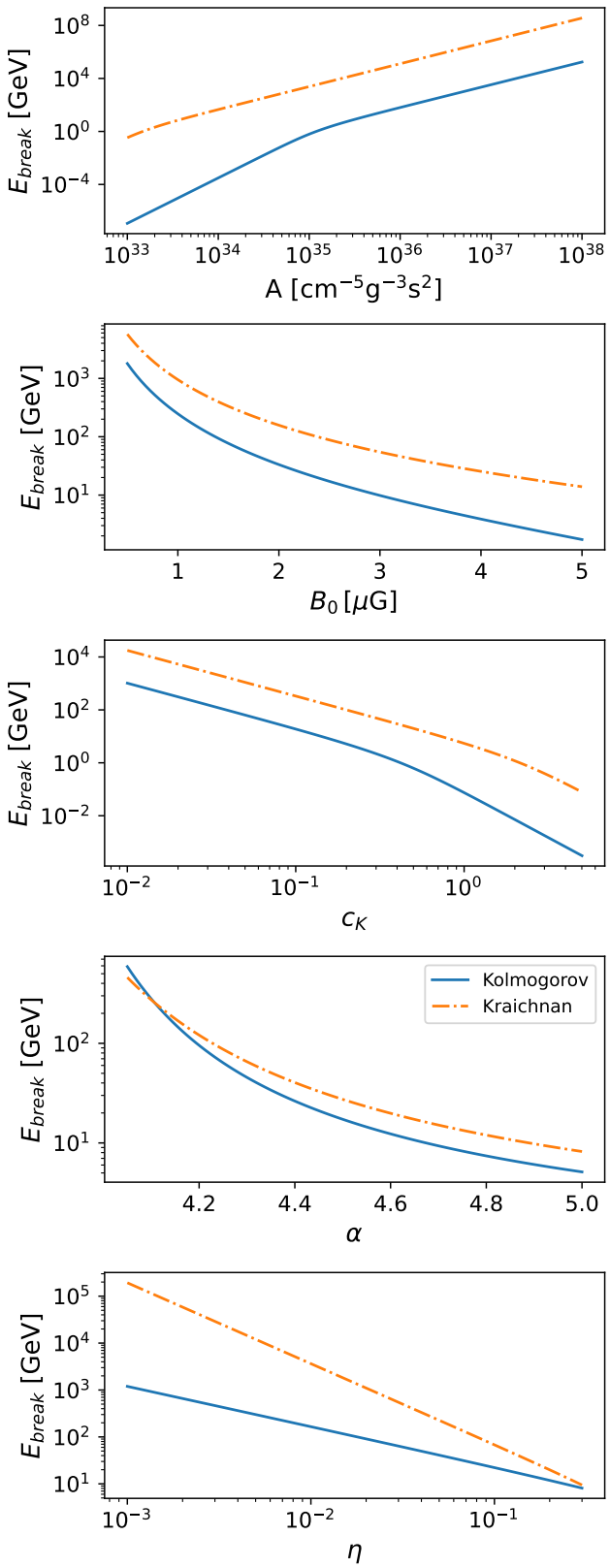

Figure 1. Comparison of the expected break energies for different values of A, η, c_K, α, and B_0 in the case of either the Kolmogorov- or Kraichnan-type of wave cascade. The respective fixed values are chosen as in Figure 2.

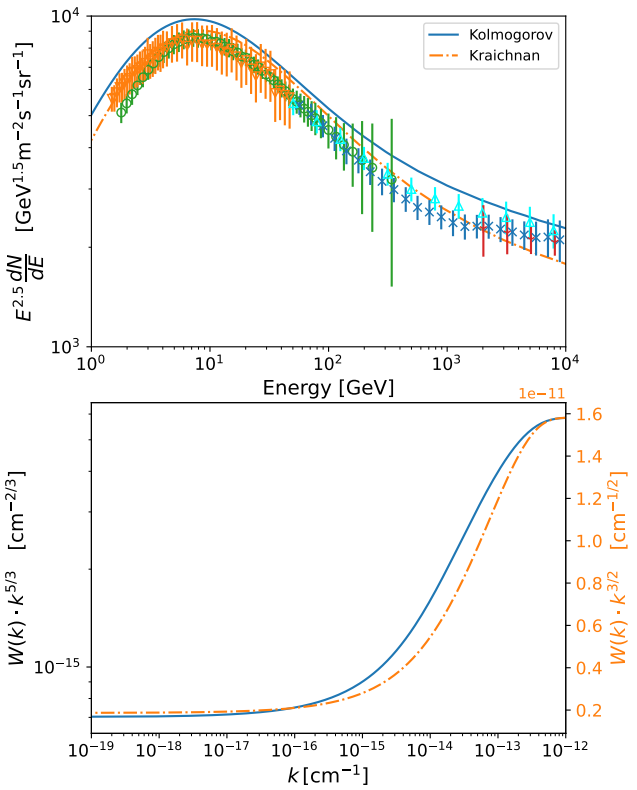

Figure 2. Comparison of the cosmic-ray fluxes (top) and wave spectra (bottom) obtained with the default parameter sets. In the Kolmogorov case, we choose $A = 10^{36}$ cm^{-5} g^{-3} s^2, $\alpha = 4.25$, $\eta = 0.03$, $v_A = 25$ km s^{-1}, $B_0 = 1.6\,\mu$G, $H = 4$ kpc, and $k_0^{-1} = 50$ pc, whereas for Kraichnan, it is $A = 10^{34.5}$ cm^{-5} g^{-3} s^2, $\alpha = 4.08$, $\eta = 0.04$, $v_A = 1$ km s^{-1}, $B_0 = 1.5\,\mu$G, $H = 4$ kpc, and $k_0^{-1} = 50$ pc.

higher turbulence level in the high-energy range is obtained.

3. *Turbulence level* η. The initial turbulence level mainly determines the high-energy regimes. With decreasing initial wave power, the streaming instability prevails to increasingly higher energies, as expected according to Equation (16). Independent of η, the final wave power approaches almost the same level at higher wavenumbers and lower energies, respectively. On the particle side, this translates into a larger particle population at higher energies due to the dependency of the diffusion coefficient (Equation (6)) on $W(k)$, the higher η, or δB, respectively, and the merging of the distribution functions toward lower energies.
4. *Influence of Alfvén speed* v_A. In comparison, the variation of the Alfvén speed v_A, which is at a fixed magnetic field B_0 associated with the variation of the background ion density n_i, has a somewhat reverse effect. While the high-energy regime is unaltered, at lower energies, the spectra spread apart. From Equation (12), upon neglecting the diffusion term—since at lower energies, advection dominates—the solution $f_0 = 3A/(2v_A\alpha)\,(p/(mc))^{-\alpha}$ can be found. Consistently, a lower speed v_A, which corresponds to a higher-density n_i, leads to a higher cosmic-ray density. The particles lose their energy until they advect with Alfvén speed. The position of the expected spectral break energy remains the same for all alterations since the latter is independent of v_A.
5. *Background magnetic field* B_0. The ambient magnetic field strength B_0 was, starting from the default value 1.6 μG, successively increased/decreased by a factor of 1.3, leading to an almost equidistant shift of wave spectra at lower energies. Increasing B_0 in our model affects only the growth rate $\Gamma_{CR} \propto B_0^{-2}$, leading to more wave excitation for smaller values of B_0. Due to the normalization of the wave spectrum to a fixed amount of turbulence, the smaller wave growth at higher B_0 is necessarily associated with a higher wave abundance at higher energies. This effect is much more pronounced in the Kraichnan case (Figure 4).
6. *Kolmogorov constant* c_K. This constant makes the energy transfer of the injected waves with wavenumber k_0 to smaller k less effective the smaller its value is. As a consequence, more waves are abundant in the energy range relevant for the cosmic rays. Thus, more cosmic rays are able to resonantly interact and excite more waves.

The plots further indicate that the estimated break energies seem to be rather underestimated.

4. Fitting the Galactic Environment Parameters

4.1. Method

In this section, we use a quantitative fitting procedure to find the parameter combination that is best suited to fit currently available observational cosmic-ray data. The use of an MCMC algorithm (D. Foreman-Mackey et al. 2013) additionally allows us to determine a range in which a parameter combination still provides a sufficiently good fit, as well as correlations between particular parameters. As suggested by D. W. Hogg et al. (2010), we assume that the deviation of the values obtained by our model, $y_{i,\mathrm{model}}(d_j)$, which is constituted by the model parameters d_j, from the given data, $y_{i,\mathrm{data}}$, with combined statistical and systematic error, $y_{i,\mathrm{err}}$, is Gaussian-distributed, so that our conditional probability function for the ith data point reads

$$p_i(y_{i,\mathrm{data}}|d_j, y_{i,\mathrm{err}}) = \frac{1}{\sqrt{2\pi y_{i,\mathrm{err}}^2}} \exp\left[-\frac{(y_{i,\mathrm{data}} - y_{i,\mathrm{model}}(d_j))^2}{2y_{i,\mathrm{err}}^2}\right]. \quad (17)$$

This choice of the maximum-entropy distribution accounts for our lack of specific knowledge about the model's outcome. The likelihood of the parameters, given the independence of each conditional probability function from another, is simply the product of all these functions, $\mathcal{L} = \prod_{i=1}^{N} p_i(y_{i,\mathrm{data}}|d_j, y_{i,\mathrm{err}})$, N being the number of data points under consideration. For the best model fit, this likelihood should be maximal. Consequently, if we take the logarithm of Equation (17), we then need to maximize

$$\ln \mathcal{L}(y_{i,\mathrm{data}}|d_j, y_{i,\mathrm{err}}) = -\frac{1}{2}\sum_{i=1}^{N}\left[\frac{(y_{i,\mathrm{data}} - y_{i,\mathrm{model}(d_j)})^2}{y_{i,\mathrm{err}}^2}\right] - \frac{1}{2}\sum_{i=1}^{N}\ln(2\pi y_{i,\mathrm{err}}^2). \quad (18)$$

Given that the number of free parameters in the model is significant, we restrict some of them to reasonable fixed values.

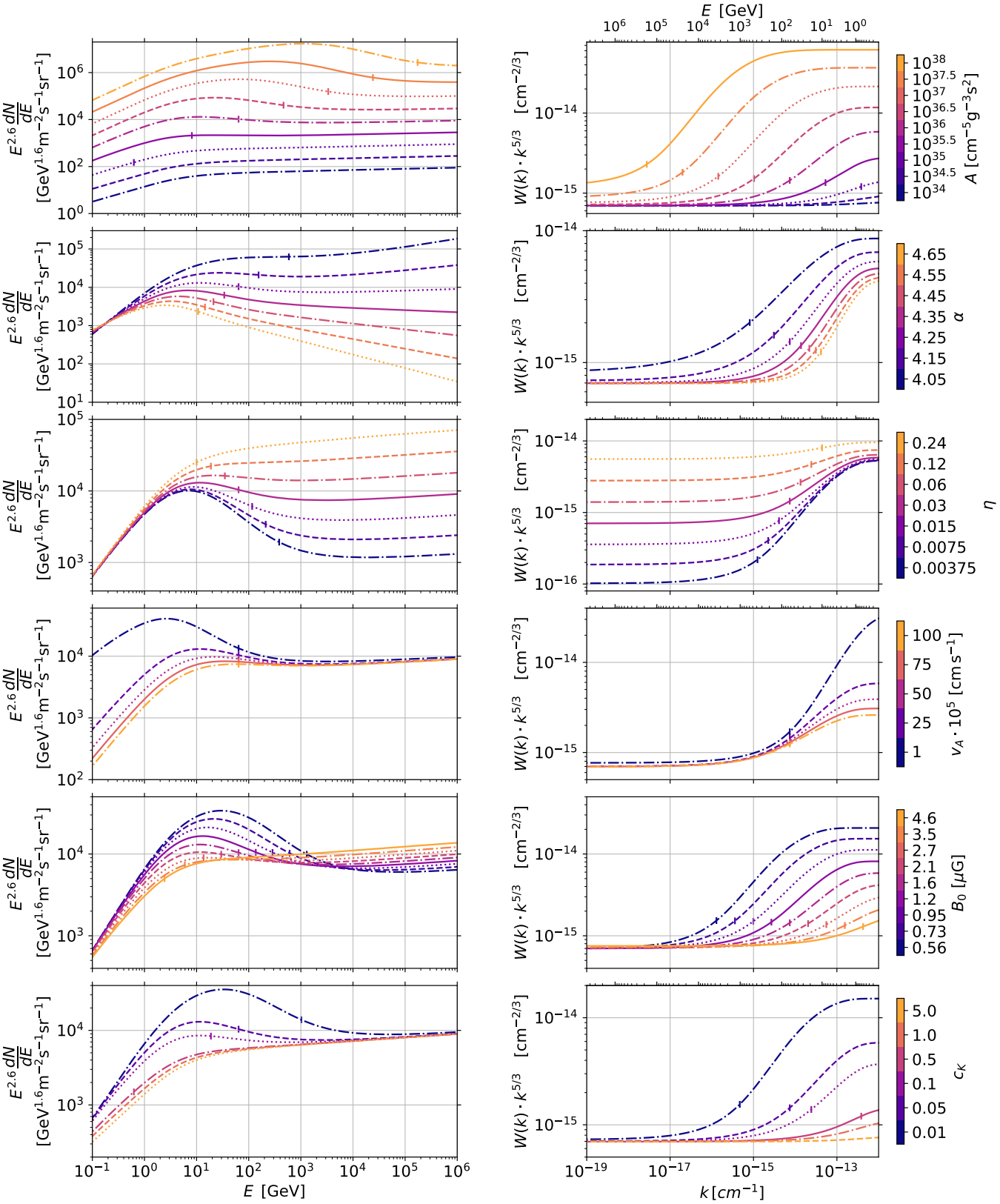

Figure 3. Kolmogorov. We vary the model parameters around the default parameter set (as specified in Figure 2), one in each row, while keeping the rest fixed. Line styles change from dashed–dotted, to dashed, to dotted, to solid with increasing parameter value. The energies for the right plots are derived as $E = (\sqrt{1 + (qB_0/(kmc^2))^2} - 1)mc^2$, except for the second-to-last row, where we varied B_0. The expected breaks according to Equation (16) are denoted by small vertical lines.

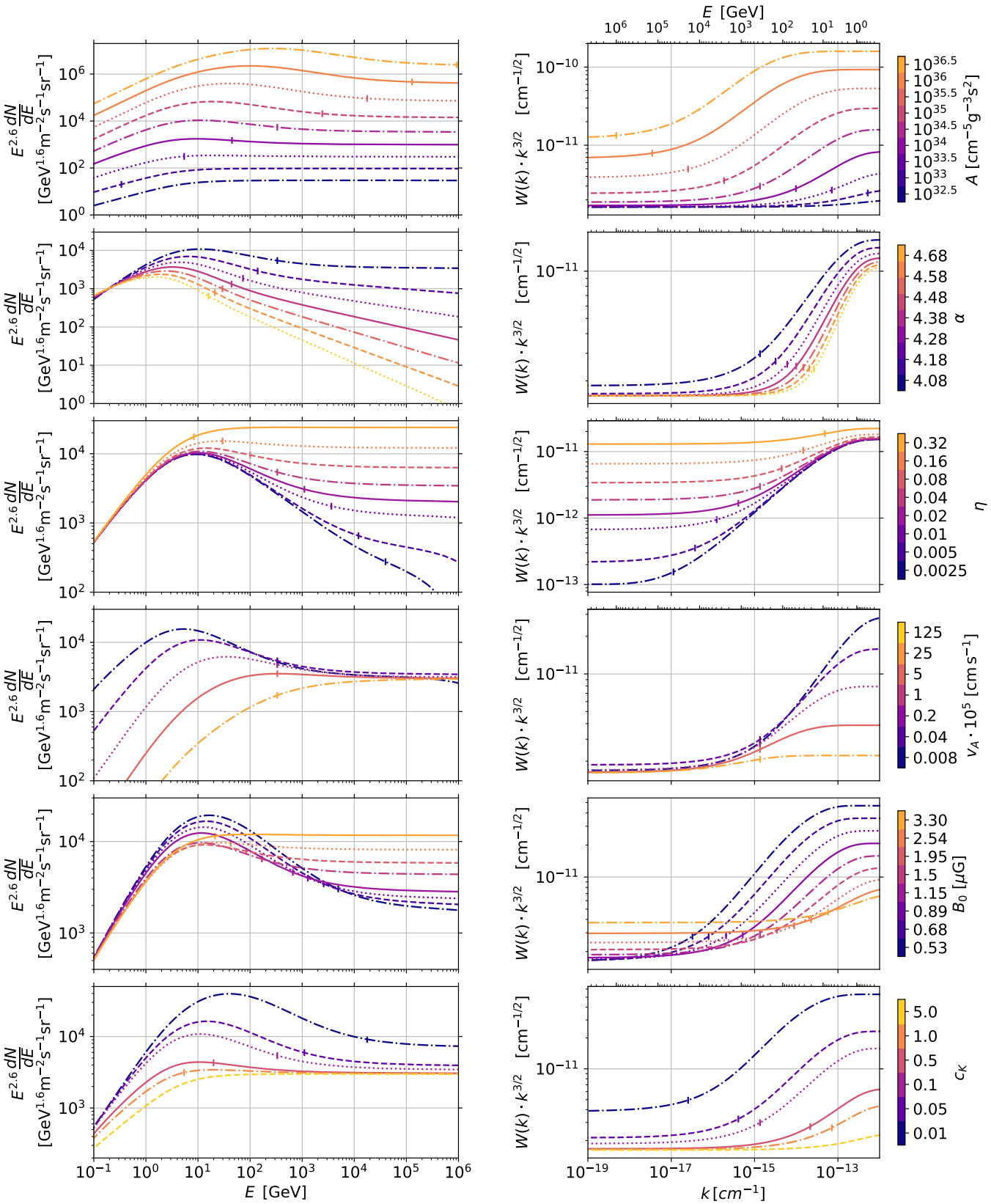

Figure 4. Kraichnan. Starting from the default values, the parameters are changed in a similar manner as in Figure 3, with the line styles kept in the same changing order. Again, small vertical lines denote the expected breaks due to the streaming instability.

Since the aim is to explain the spectral break observed at about 300 GeV, we choose the CALET data (O. Adriani et al. 2022) to be our input values, $y_{i,\mathrm{data}}$. Due to the small error bars of the AMS-02 data, the fitting of the lower-energy part of the cosmic-ray spectrum would have prevailed with a less prioritized fit of the spectral break as a consequence, which

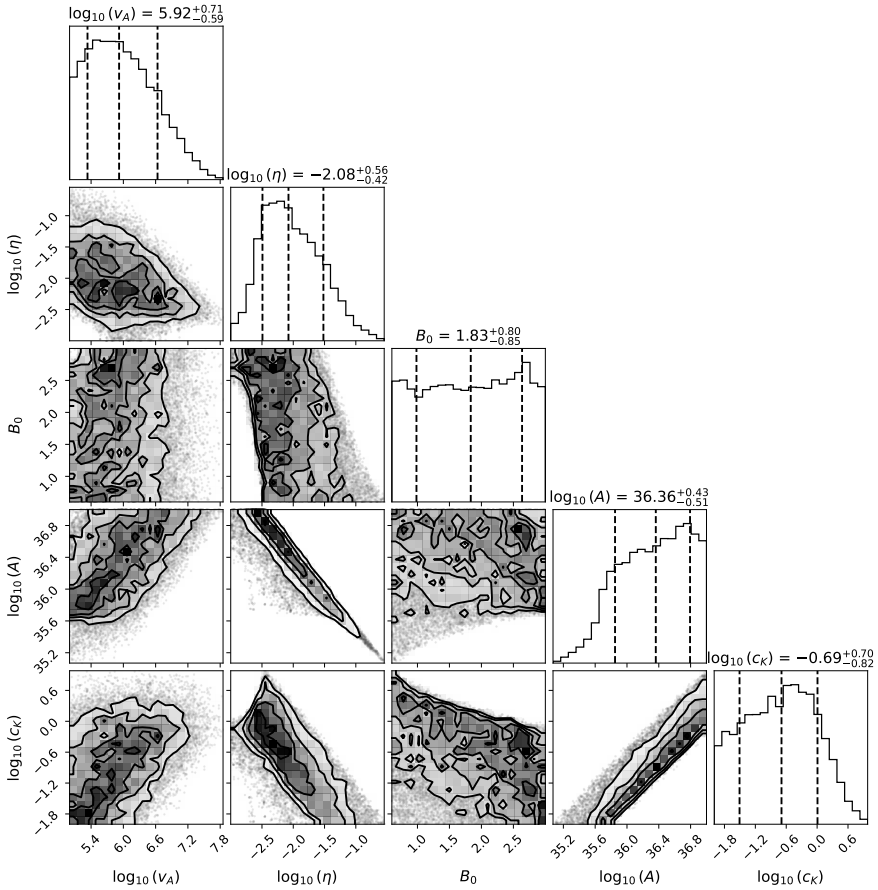

Figure 5. Corner plot of our parameters for a Kolmogorov-type cascade. On the diagonal, the marginalized distributions of the Alfvén speed v_A, turbulence measure η, mean magnetic field B_0, cosmic-ray normalization constant A, and Kolmogorov constant c_K are displayed, with the dashed lines denoting the 68% credible areas. The remaining panels show the marginalized two-dimensional distributions.

is why we spare it here. The spectral index α is set such that it matches the slope of the CALET data above the break in the diffusion-dominated limit, where $f(p) \propto p^{-\alpha}/D(p)$. In case of the Kolmogorov phenomenology, this implies $\alpha = 4.25$, while Kraichnan suggests $\alpha = 4.08$. Both choices are in agreement with recent research advocating for cosmic-ray spectra steeper than p^{-4} (e.g., A. Bell 2013). The injection scale k_0^{-1} of the turbulence is fixed to 50 pc, since this parameter has a similar effect as η due to the normalization of the background turbulence (Equation (7)). The halo height is fixed to a typical value of $H = 4$ kpc. On the remaining parameters, we impose uniform priors:

$$\pi(d_j) = \begin{cases} \dfrac{1}{d_{j,\max} - d_{j,\min}}, & \text{for } d_{j,\min} < d_j < d_{j,\max}, \\ 0, & \text{otherwise.} \end{cases} \tag{19}$$

We determine the ranges of the parameters based on the quantitative parameter study performed in Section 3. The optimal value for the Alfvén speed v_A is assumed to be found in a range $[10^5, 10^8]\,\mathrm{cm\,s^{-1}}$, the turbulence level $\eta \in [10^{-3}, 10^1]$, the mean magnetic field $B_0 \in [0.6, 3.0]\,\mu\mathrm{G}$, the Kolmogorov constant $c_K \in [10^{-2}, 10^1]$, and the cosmic-ray injection factor $A \in [10^{34}, 10^{37}]\,\mathrm{cm^{-5}\,g^{-3}\,s^2}$ in the Kolmogorov case and $v_A \in [10^3, 10^5]\,\mathrm{cm\,s^{-1}}$, $\eta \in [10^{-3}, 10^1]$, $B_0 \in [0.6, 3.0]\,\mu\mathrm{G}$, $c_K \in [10^{-2}, 10^1]$, and $A \in [10^{33.5}, 10^{35.5}]\,\mathrm{cm^{-5}\,g^{-3}\,s^2}$ in the Kraichnan case. The posterior probability distribution according to Bayesian inference is

$$P(y_{i,\mathrm{model}}|d_j, y_{i,\mathrm{err}}) \propto \mathcal{L}(y_{i,\mathrm{data}}|d_j, y_{i,\mathrm{err}})\,\pi(d_j), \tag{20}$$

which needs to be maximized. With regard to numerical stability, we maximize the logarithm of this expression.

4.2. Results

Figures 5 and 6 show the resulting corner plots, i.e., one- and two-dimensional projections of the posterior probability, the product of our conditional probability function and the priors. For these, we used the corner package (D. Foreman-Mackey 2016) available for Python. The solid lines enclosing differently sized and shaded areas denote the 1σ, 2σ, and 3σ intervals. We find the most prominent correlations between the turbulence level η and the normalization constant A and between η and the Kolmogorov constant c_K, and thus also between A and c_K. Increasing A or c_K is associated with a decrease of η, which is reasonable since the former two parameter variations lead to more wave excitation that needs to be balanced by a decrease of preexisting turbulence. Similarly plausible, A and c_K are correlated in such a way that increasing A requires an increase of c_K. The ambient magnetic field strength appears to be the least constrained parameter. Table 1 summarizes the median values resulting from the MCMC analysis and the respective 1σ intervals. Due to the various

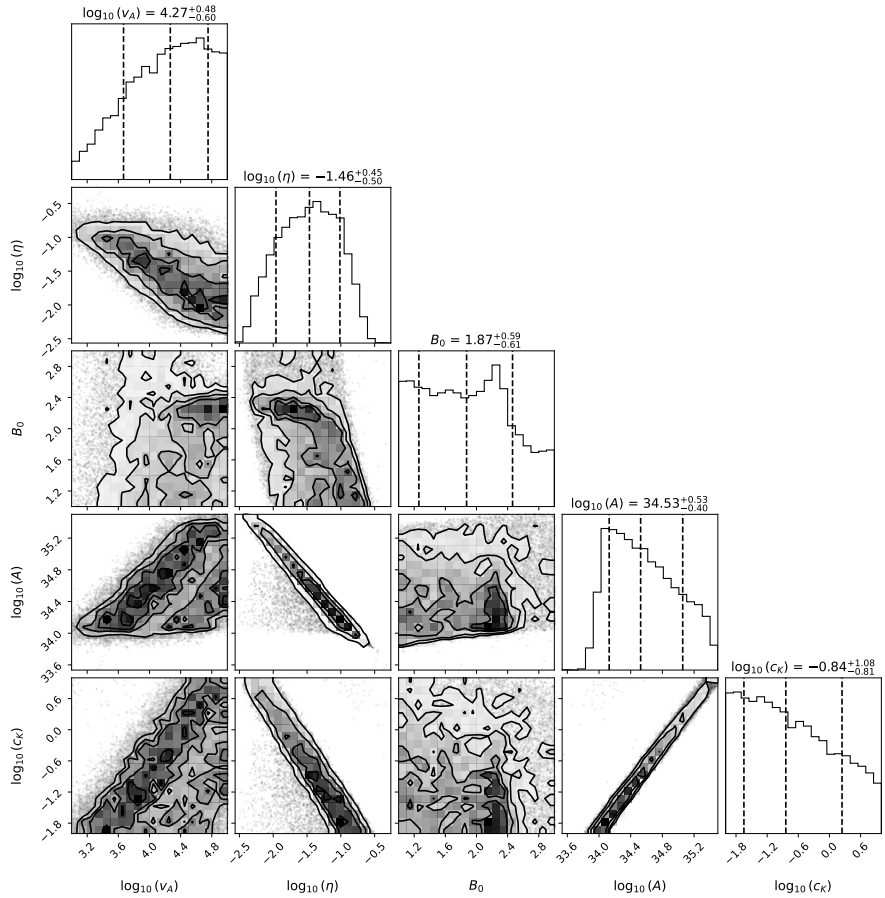

Figure 6. Corner plot for a Kraichnan-type cascade. As in Figure 5, the one-dimensional marginalized distributions with the 68% credible areas are shown, as well as the marginalized two-dimensional distributions.

Table 1
Summary of All Model Parameters, the Allowed Ranges We Used, and the Median Results with Their 1σ Intervals

Parameter	Symbol	Unit	Tested Range		Median Value		1σ Interval	
			Kolmogorov	Kraichnan	Kolmogorov	Kraichnan	Kolmogorov	Kraichnan
Alfvén speed	$\log_{10} v_A$	cm s^{-1}	[5, 8]	[3, 5]	5.92	4.27	[5.33, 6.63]	[3.67, 4.75]
Halo height	H	kpc	4	4	⋯	⋯	⋯	⋯
Turbulence level	$\log_{10}\eta$	⋯	[−3, 1]	[−3, 1]	−2.08	−1.46	[−2.50, −1.52]	[−1.96, −1.01]
Injection scale	k_0^{-1}	pc	50	50	⋯	⋯	⋯	⋯
Background field	B_0	μG	[0.6, 3.0]	[0.6, 3.0]	1.83	1.87	[0.98, 2.63]	[1.26, 2.46]
Injection factor	$\log_{10} A$	cm^{-5} g^{-3} s^2	[34, 37]	[33.5, 35.5]	36.36	34.53	[35.85, 36.79]	[34.13, 35.06]
Injection slope	α	⋯	4.25	4.08	⋯	⋯	⋯	⋯
Kolmogorov constant	$\log_{10} c_K$	⋯	[−2, 1]	[−2, 1]	−0.69	−0.84	[−1.51, 0.01]	[−1.65, 0.24]

correlations that the parameters exhibit and the fact that most of the one-dimensional marginalized distributions are not symmetrical, using the median value for each of them in our model does not provide the best fit to the cosmic-ray data. To account for the model uncertainty, we construct the 1σ variation of the likelihood around the overall minimum using Wilk's theorem. The resulting min–max variation of the models is shown in Figure 7. We find a stronger break in the Kolmogorov case but with an accompanying overshooting of the lower-energy part of the cosmic-ray spectrum data, since the datasets for the lower-energy regime were not considered in our MCMC procedure, but only the CALET data ranging from ∼5 GeV to 10 TeV. Both fits tend to lie beneath the data points at higher energies, since the spectral breaks are softer than the data would suggest. The plotted AMS-02 and PAMELA data have been corrected for the solar modulation using a force-field approximation (L. J. Gleeson 1968) with the modulation parameter determined by each experiment, respectively. The error bars are given as the combined statistical and systematic errors.

5. Discussion and Conclusions

We carried out an MCMC analysis of a simple model for Galactic cosmic-ray transport, self-consistently including the streaming instability. From this procedure, we obtain optimal parameter ranges that might help to constrain the actual physical values for the Milky Way. Since we only allowed for

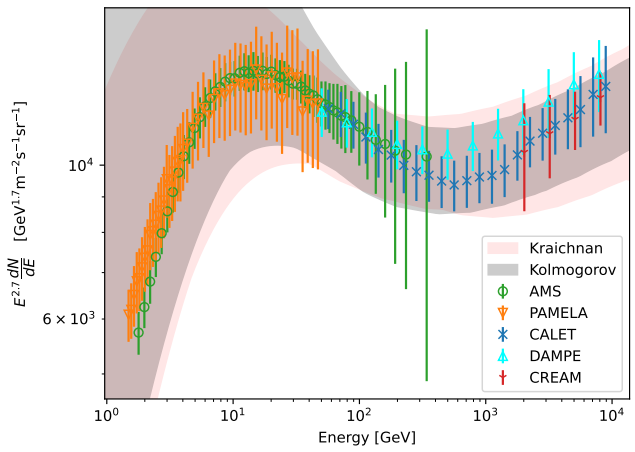

Figure 7. The 1σ variation of the likelihood around the overall minimum for the Kolmogorov case (gray) and the Kraichnan case (red) compared to data from AMS-02 (M. Aguilar et al. 2021), PAMELA (O. Adriani et al. 2011), CALET (O. Adriani et al. 2022), DAMPE (Q. An et al. 2019), and CREAM (Y. S. Yoon et al. 2011).

the streaming instability to occur, disregarding further possible excitation or damping processes, this model can be considered as an attempt to explore the plausibility of this very effect as a cause of the observed spectral break. Furthermore, since we reduced the complexity to one dimension, the values obtained may be considered as a local value averaged across the Galactic halo.

The median values in the Kolmogorov case suggest a background ion density of $n_i = 0.23\,\mathrm{cm}^{-3}$, and the case of Kraichnan yields $n_i = 480\,\mathrm{cm}^{-3}$. In fact, the MCMCs indicate allowed ranges of $n_i \in [0.0025, 7.2]$ and $n_i \in [23.9, 13160]\,\mathrm{cm}^{-3}$, respectively. Values such as the latter are only realized in environments where ionization is far from complete, so ion-neutral damping must then be taken into account, and our approach, therefore, is insufficient. The former value agrees well with, e.g., K. Ferrière (1998), who modeled the interstellar hydrogen density and found densities of up to $\sim$0.2 cm^{-3} for the warm ionized medium.

In regard to the mean magnetic field B_0, both cases do not show clear preferences for a certain value, since the marginalized distributions are more or less flat. The suggested values of about 1.8 μG are, therefore, simply the median of the tested ranges. Local measurements of the heliosheath flow (M. Opher et al. 2009), synchrotron emission (K. Beuermann et al. 1985), or γ-ray data (A. W. Strong et al. 2000) indicate values of 4 -6 μG, but lower strengths around 1 μG are also found from rotation measurements of pulsars (R. J. Rand & A. G. Lyne 1994).

The turbulent component of the magnetic field is afflicted with more uncertainty. Though in spiral galaxies, it is assumed to be stronger than the ordered field, some references support lower values for our Galaxy. P. Reichherzer et al. (2022) use a turbulence value of $\delta B/B_0 \approx 0.5$ in their analysis, which was scaled down due to a likely overestimation, as J. Becker Tjus & L. Merten (2020) argue. Here, the turbulence measure $\eta = \delta B^2/B_0^2$ is determined by the normalization Equation (7), which directly relates η to k_0, making them codependent parameters. With fixed B_0, the variation of k_0^{-1} therefore has a direct effect on the value of η. The injection scale k_0^{-1}, in turn, is uncertain and typically estimated to be in a range of 10 -100 pc (e.g., M. Haverkorn et al. 2008; C. Evoli et al. 2018). Our η-values give us turbulence levels of $\delta B/B_0 = 0.091$ and $\delta B/B_0 = 0.19$ for Kolmogorov and Kraichnan, respectively. Taking into account the uncertainty of k_0^{-1}, our analysis allows ranges of $\delta B/B_0$ of [0.064, 0.2] and [0.13, 0.42], respectively. Those values are slightly below the values derived by P. Reichherzer et al. (2022).

The cosmic-ray injection factor A obtained within this model appears to be of a reasonable order of magnitude as well. The energy released by SNe is assumed to be about 10^{51} erg (R. A. Chevalier 1977), of which about 10% is converted into kinetic energy of protons (C. D. Dermer & G. Powale 2013). The Galactic SN rate is estimated to be $1/(36\,\mathrm{yr})$ (M. Kachelrieß & V. Mikalsen 2025), $1/(40\,\mathrm{yr})$ (G. A. Tammann et al. 1994), or even between $1/50$ and $1/(100\,\mathrm{yr})$ (B. C. Reed 2005). Given a Galactic radius $R_d \approx 10$ kpc, the normalization of A according to Equation (3) would be of the order of $10^{36}\,\mathrm{cm}^{-5}\,\mathrm{g}^{-3}\,\mathrm{s}^2$. If, as a rough estimate, we allow for ranges $E_{\mathrm{SN}} \in [5 \times 10^{50}, 10^{51}]$ erg, $\xi_{\mathrm{CR}} \in [5, 15]\%$, $R_d \in [5, 20]$ kpc, and $\mathcal{I}(\alpha) \in [43, 248]$, since α is in the range $\sim$[4.05, 4.3], we obtain a range for the injection factor of $A \in [1 \times 10^{34}, 2 \times 10^{37}]\,\mathrm{cm}^{-5}\,\mathrm{g}^{-3}\,\mathrm{s}^2$, well consistent with both of our results.

The Kolmogorov constant c_{K} is associated with some uncertainty and, partly, not used consistently throughout the literature. It commonly appears in the expression relating the wave energy and wavenumber, $W = \tilde{c}_{\mathrm{K}}\,\epsilon^{2/3}k^{-5/3}$, where $\epsilon = -D_{kk}\,\nabla\,W$. A. Beresnyak (2011) performs MHD simulations and finds $\tilde{c}_{\mathrm{K}} = 4.2$, P. K. Yeung & Y. Zhou (1997) yield $\tilde{c}_{\mathrm{K}}$ values of 0.60 and 0.53 for the one- and three-dimensional energy spectra, K. R. Sreenivasan (1995) obtains $\tilde{c}_{\mathrm{K}} = 0.53$, and a study by M. K. Verma et al. (1996) reports $\tilde{c}_{\mathrm{K}} = 3.6$. By inserting our diffusion coefficient, Equation (9), and comparing our expression with the ansatz in which $W \propto \tilde{c}_{\mathrm{K}}$, we assume $c_{\mathrm{K}} = (\tilde{c}_{\mathrm{K}})^{-3/2}$, so that our result for the Kolmogorov case, $c_{\mathrm{K}} \approx 0.37$, is in the expected order of magnitude. In case of a Kraichnan-like cascade, numerical simulations were carried out by D. Biskamp & H. Welter (1989) that indicate $\tilde{c}_{\mathrm{K}} = 1.8 \pm 0.2$. W. H. Matthaeus & Y. Zhou (1989) suggest a relation of the Kolmogorov constant and the "Kraichnan constant" and conclude $\tilde{c}_{\mathrm{K}} = 1.22 - 1.87$. Since in this case, the relation is $W \propto \tilde{c}_{\mathrm{K}}\,k^{-3/2}$, our constant would be calculated as $c_{\mathrm{K}} = (\tilde{c}_{\mathrm{K}})^{-2}$. The best-fit result from the MCMC analysis yields $c_{\mathrm{K}} \approx 1.41$, corresponding to $\tilde{c}_{\mathrm{K}} = 1.99$.

In both turbulence cases, the break at a few hundred GeV is similar, and the stronger softening of the Kolmogorov spectrum is in better accordance with other data, such as DAMPE. The overshooting in the lower-energy regime might allude to a spectral break in the particles' source spectrum, q_{CR}, as indicated by MHD simulations (e.g., S. Das et al. 2024).

So, in summary, our MCMC analysis shows that the streaming instability, in combination with a Kolmogorov- as well as a Kraichnan-like cascade, is capable of self-consistently causing a spectral break that resembles the one emerging at a few hundred GeV in available cosmic-ray data. The associated values for the various model parameters favor the former phenomenology.

Acknowledgments

This work was supported by the Deutsche Forschungsgemeinschaft within the Collaborative Research Center SFB1491 (project No. 445052434) and by the European Union —

NextGenerationEU RRF M4C2 1.1 under grant PRIN-MUR 2022TJW4EJ.

Appendix
Pitch-angle-dependent Diffusion

Within this work, the resonance condition for the wave–particle interaction $k = 1/r_{\rm L} = qB_0/(pc)$ has been applied. This expression is a simplification, as in general, the component parallel to the magnetic field is crucial, $k_{\parallel}$. Therefore, the resonance condition should more precisely read

$$k_{\rm res} = \frac{qB_0}{cp\mu}, \tag{A1}$$

μ being the cosine of the particle pitch angle. Recently, M. A. Malkov et al. (2024) discussed that a proper treatment of the pitch-angle-dependent diffusion will smear out any sharp breaks that occur in the wave spectrum. In the following, we compare the smoothing introduced by the pitch-angle dependence with the natural smoothness appearing in our model due to the fact that only smooth distribution functions are considered.

As a baseline model, we use the median values for the Kolmogorov case introduced in Table 1 for comparison. In Figure 8 the resulting wave power spectrum is shown. Using this and the resonant scattering condition introduced before, we compute the diffusion coefficient following Equation (6). The resulting diffusion coefficient is displayed in Figure 9. To estimate the smoothness in the break of the median model, we fit the energy dependence of the diffusion coefficient with a smooth broken power law (BPL):

$$D(E) = D_0\left(\frac{E}{E_{\rm br}}\right)^{\gamma_1}\cdot\left(1+\left(\frac{E}{E_{\rm br}}\right)^{1/\delta}\right)^{\delta(\gamma_2-\gamma_1)}. \tag{A2}$$

The fit is restricted to the energy range $1 \leqslant E/\mathrm{GeV} \leqslant 10^5$ to avoid contamination from the not-fully-relativistic regime. The resulting fitting parameters are shown in Table 2.

In the next step, we estimate the smoothness introduced by the pitch-angle dependence in the resonant scattering condition. Therefore, we approximate the wave spectrum with a sharp BPL,

$$W(k) = W_0\cdot\begin{cases}(k/k_{\rm br})^{a_2} & \text{for } k \leqslant k_{\rm br},\\ (k/k_{\rm br})^{a_1} & \text{for } k_{\rm br} \leqslant k \leqslant 50k_{\rm br},\\ 50^{a_1}\,(k/50k_{\rm br})^{a_2} & \text{for } k > 50k_{\rm br},\end{cases} \tag{A3}$$

where the break wavenumber $k_{\rm br} = 1/r_L(E_{\rm br})$ and the slopes $a_i = \gamma_i - 2$ are obtained from the fitted diffusion coefficient (see Table 2). The second break at $k = 50\,k_{\rm br}$ is introduced to prevent overshooting in the nonrelativistic regime but does not affect energies $E \gtrsim 1$ GeV. The normalization W_0 is chosen in such a way that the final diffusion coefficient matches the median model at 100 TeV. With this wave spectrum and the pitch-angle-dependent resonance condition, Equation (A1), we compute the diffusion coefficient following M. A. Malkov et al. (2024):

$$D(p) = \frac{cB^2p^2}{m^2\omega_c^2}\int\frac{|\mu|(1-\mu^2)}{W(k=qB/cp\mu)}d\mu. \tag{A4}$$

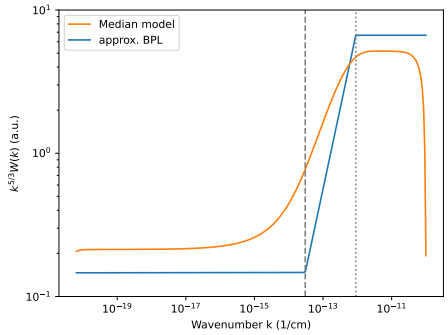

Figure 8. Wave spectrum in the median model obtained in the Kolmogorov case with the values given in Table 1. In order to compare the effect of the natural smoothness to the smearing due to the pitch-angle-dependent resonance, the spectrum is approximated with a sharp (double) BPL as in Equation (A3).

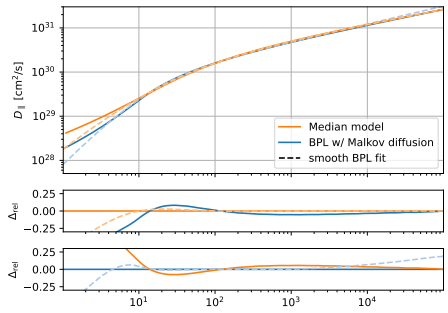

Figure 9. Comparison of the diffusion coefficient as used in this work (median model) to the approximated BPL wave spectrum (see Figure 8) on which the pitch-angle-dependent resonance from M. A. Malkov et al. (2024) was applied. To assess the smoothness of both curves, they were fitted with smooth BPLs following Equation (A2) (dashed lines). The two lower panels show the relative differences of these fits to their corresponding models (middle panel: median model; bottom panel: BPL model) to measure the goodness of both fits.

Table 2
Fitting Parameter of the Smooth BPL (Following Equation (A2)) for the Diffusion Coefficients Shown in Figure 9

Parameter	Median Model	BPL Model
$E_{\rm br}$/GeV	17 ± 5	13.2 ± 0.9
γ_1	1.457 ± 0.12	1.76 ± 0.05
γ_2	0.3337 ± 0.001	0.406 ± 0.002
δ	1.60 ± 0.03	0.99 ± 0.02

Afterward, we also fit the resulting diffusion coefficient with a smooth BPL.[5] The diffusion coefficient and its fit is shown in Figure 9, and the respective fitting values are summarized in Table 2.

To compare the smoothness introduced by the pitch-angle-dependent resonance with the naturally arising smoothness in our model, we need to compare the smoothness parameters δ of both fits. The median model has a larger smoothness ($\delta = 1.6$) than the BPL with the pitch-angle effect ($\delta = 0.99$). Therefore, we conclude that the smoothing due to the pitch-angle dependence is only a secondary effect and would not add up significantly to the natural smoothness. As the computation

[5] To achieve a better-fitting result, we restrict the energy range to $1 \leqslant E/\mathrm{GeV} \leqslant 10^3$.

of the diffusion coefficient including the pitch-angle dependence would introduce an additional integral, and subsequently increase the overall computation time, we decide to remain with the simplified resonance condition for the main analysis.

ORCID iDs

Linh Han Thanh https://orcid.org/0000-0002-5291-1645
Julien Dörner https://orcid.org/0000-0001-6692-6293
Julia Becker Tjus https://orcid.org/0000-0002-1748-7367
Horst Fichtner https://orcid.org/0000-0002-9151-5127
Elena Amato https://orcid.org/0000-0002-9881-8112

References

Abreu, P., Aglietta, M., Albury, J. M., et al. 2021, EPJC, 81, 966
Adriani, O., Akaike, Y., Asano, K., et al. 2022, PhRvL, 129, 101102
Adriani, O., Barbarino, G. C., Bazilevskaya, G. A., et al. 2011, Sci, 332, 69
Aguilar, M., Aisa, D., Alpat, B., et al. 2015, PhRvL, 114, 171103
Aguilar, M., Ali Cavasonza, L., Ambrosi, G., et al. 2021, PhR, 894, 1
Aloisio, R., & Blasi, P. 2013, JCAP, 2013, 001, 2013JCAP...07..001A
An, Q., Asfandiyarov, R., Azzarello, P., et al. 2019, SciA, 5, eaax3793
Becker Tjus, J., & Merten, L. 2020, PhR, 872, 1
Bell, A. 2013, APh, 43, 56
Beresnyak, A. 2011, PhRvL, 106, 075001
Beuermann, K., Kanbach, G., & Berkhuijsen, E. M. 1985, A&A, 153, 17
Bhadra, S., Thoudam, S., Nath, B. B., & Sharma, P. 2025, ApJ, 989, 74
Biermann, P. L., Becker, J. K., Dreyer, J., et al. 2010, ApJ, 725, 184
Biskamp, D., & Welter, H. 1989, PhFlB, 1, 1964
Blasi, P., & Amato, E. 2012, JCAP, 2012, 010
Blasi, P., Amato, E., & Serpico, P. D. 2012, PhRvL, 109, 061101
Chevalier, R. A. 1977, ARA&A, 15, 175
Das, S., Brose, R., Pohl, M., Meyer, D. M.-A., & Sushch, I. 2024, A&A, 689, A9
Dermer, C. D., & Powale, G. 2013, A&A, 553, A34
De Rújula, A. 2019, PhLB, 790, 444
Evoli, C., Blasi, P., Morlino, G., & Aloisio, R. 2018, PhRvL, 121, 021102
Ferrière, K. 1998, ApJ, 497, 759
Foreman-Mackey, D. 2016, JOSS, 1, 24
Foreman-Mackey, D., Hogg, D. W., Lang, D., & Goodman, J. 2013, PASP, 125, 306
Gleeson, L. J. 1968, PASA, 1, 130
Greisen, K. 1966, PhRvL, 16, 748
Haverkorn, M., Brown, J. C., Gaensler, B. M., & McClure-Griffiths, N. M. 2008, ApJ, 680, 362
Hogg, D. W., Bovy, J., & Lang, D. 2010, arXiv:1008.4686
Kachelrieß, M., & Mikalsen, V. 2025, CoPhC, 311, 109537
Kampert, K.-H. 2013, BrJPh, 43, 375
Kulsrud, R., & Pearce, W. P. 1969, ApJ, 156, 445
Leith, C. E. 1967, PhFl, 10, 1409
Liu, W., Yao, Y.-h., & Guo, Y.-Q. 2018, ApJ, 869, 176
Malkov, M. A., Moskalenko, I. V., Diamond, P. H., & Cao, M. 2024, AdSpR, 74, 4264
Matthaeus, W. H., & Zhou, Y. 1989, PhFlB, 1, 1929
Miller, J. A., & Roberts, D. A. 1995, ApJ, 452, 912
Opher, M., Bibi, F. A., Toth, G., et al. 2009, Natur, 462, 1036
Pan, X., & Yuan, Q. 2023, RAA, 23, 115002
Potgieter, M. S. 1998, SSRv, 83, 147
Qian, X.-L., Sun, H.-Y., Nie, L., et al. 2025, ApJ, 989, 96
Rand, R. J., & Lyne, A. G. 1994, MNRAS, 268, 497
Recchia, S., & Gabici, S. 2024, A&A, 692, A20
Reed, B. C. 2005, AJ, 130, 1652
Reichherzer, P., Merten, L., Dörner, J., et al. 2022, SNAS, 4, 15
Shalchi, A. 2009, APh, 31, 237
Silver, E., & Orlando, E. 2024, ApJ, 963, 111
Skilling, J. 1971, ApJ, 170, 265
Sreenivasan, K. R. 1995, PhFl, 7, 2778
Strong, A. W., Moskalenko, I. V., & Reimer, O. 2000, ApJ, 537, 763
Tammann, G. A., Loeffler, W., & Schroeder, A. 1994, ApJS, 92, 487
Thoudam, S., & Hörandel, J. R. 2014, A&A, 567, A33
Tomassetti, N. 2012, ApJL, 752, L13
Verma, M. K., Roberts, D. A., Goldstein, M. L., Ghosh, S., & Stribling, W. T. 1996, JGR, 101, 21619
Virtanen, P., Gommers, R., Oliphant, T. E., et al. 2020, NatMe, 17, 261
Yeung, P. K., & Zhou, Y. 1997, PhRvE, 56, 1746
Yoon, Y. S., Ahn, H. S., Allison, P. S., et al. 2011, ApJ, 728, 122
Zatsepin, G. T., & Kuz'min, V. A. 1966, JETPL, 4, 78
Zhou, Y., & Matthaeus, W. H. 1990, JGRA, 95, 14881